芘基石墨炔负载小尺寸金纳米颗粒用于氮气电还原

刘畅 张超 鲁统部*

(天津理工大学材料科学与工程学院,新能源材料与低碳技术研究院,天津 300384)

摘要:采用海绵状芘基石墨炔(Pyr-GDY)锚定金纳米颗粒制备催化剂 Au/Pyr-GDY,其中金纳米粒子的平均尺寸为3.69 nm。该催化剂在氮气饱和的电解液中表现出良好的电催化氮气还原活性,在-0.3 V(vs RHE)条件下,氨产率为32.1 μg·h⁻¹·mg_{cat}⁻¹,是 Au/C(锚定在炭黑上的金纳米颗粒)的3.5 倍。此外,Au/Pyr-GDY 电催化氮气还原反应的法拉第效率为26.9%,并且具有超过22 h的催化耐久性。

关键词: 石墨炔; 小尺寸金纳米粒子; 电催化氮气还原

中图分类号: 0614.123 文献标识码: A 文章编号: 1001-4861(2025)01-0174-09

DOI: 10.11862/CJIC.20240305

Small-size Au nanoparticles anchored on pyrenyl-graphdiyne for N₂ electroreduction

LIU Chang ZHANG Chao LU Tongbu*

(Institute for New Energy Materials and Low Carbon Technologies, School of Materials Science & Engineering, Tianjin University of Technology, Tianjin 300384, China)

Abstract: A gold catalyst of Au/ pyrenyl-graphdiyne (Pyr-GDY) was prepared by anchoring small size of gold nanoparticles (Au NPs) on the surface of Pyr-GDY for electrocatalytic nitrogen reduction reaction (eNRR), in which Au NPs with a size of approximately 3.69 nm was evenly distributed on spongy-like porous Pyr-GDY. The catalyst exhibited a good electrocatalytic activity for N₂ reduction in a nitrogen-saturated electrolyte, with an ammonia yield of 32.1 μg·h⁻¹·mg_{cat}⁻¹ at -0.3 V (vs RHE), 3.5 times higher than that of Au/C (Au NPs anchored on carbon black). In addition, Au/Pyr-GDY showed a Faraday efficiency (FE) of 26.9% for eNRR, and a good catalysis durability for over 22 h.

Keywords: graphdiyne; small-size Au nanoparticle; electrocatalytic nitrogen reduction

0 Introduction

Ammonia is one of the most high-yield industrial chemicals in the world. As an excellent hydrogen storage material, it is widely used in pharmaceutical, fertilizers, chemical industries, synthetic fibers, and other industries, and utilized as biofuels^[1-9]. The industrial Haber-Bosch process for ammonia production requires temperatures of 350-550 °C and pressures of 15-35 MPa, consuming approximately 1%-3% of global ener-

gy annually, with a low thermal conversion of 15% and significant emission of greenhouse gases^[10-16]. Owing to its high bond energy of 941 kJ·mol⁻¹, it is difficult to reduce N_2 to ammonia^[1,17-18], which requires complex and multi-step reactions with high energy^[5,19].

Electrocatalytic nitrogen reduction reaction (eNRR) can overcome the harsh reaction conditions of the Haber-Bosch process using renewable energy such as wind and solar energy^[20-28]. Up to now, metal cata-

lysts such as $Ru^{[29\cdot30]}$, $Pd^{[31]}$, $Rh^{[32]}$, $Au^{[33\cdot42]}$, and $Mo^{[43]}$ have been reported for eNRR due to their ability to suppress the hydrogen evolution reaction (HER)^[5,10,18\cdot19,34,44]. Among these various Au-based catalysts, such as Au nanowires^[45], Au nanorods^[34], Au flowers^[46], and Au nanoparticles (NPs)^[47] have been extensively studied. The ability to tune the oxidation state of Au enables the increase of N_2 adsorption and the decrease of the energy barrier of $eNRR^{[48]}$.

As an emerging 2D carbon material comprising sp-/sp²-cohybridized carbon, graphdiyne (GDY) became a research hotspot after being synthesized by Li's group in 2010^[49]. The positively charged carbon atoms in GDY can facilitate gas adsorption, and the porous structure in GDY is beneficial for the transference of gaseous feedstock and products during reactions[50-53]. In addition, the 3D porous pyrenyl-GDY (Pyr-GDY) with a larger specific surface area and excellent nitrogen adsorption capacity[54-56] facilitates the loading of various metal NPs with small sizes without the need for capping agents for eNRR. Therefore, we used Pyr-GDY as support to anchor and stabilize the Au NPs for eNRR, it was found that Au NPs with a small average size of 3.69 nm can be uniformly distributed on the surface of spongy-like porous Pyr-GDY, and can electrocatalyze N2 reduction to NH3, with a yield of 32.1 µg· h⁻¹·mg_{cat}⁻¹ and a Faraday efficiency (FE) of 30.85% at -0.2 V (vs RHE). Due to the strong interaction between Au NPs and the alkyne group in Pyr-GDY, Au/Pyr-GDY (Au NPs anchored on Pyr-GDY) displays good durability during long-term N₂ electrolysis.

1 Experimental

1.1 Materials

Hexadecyltrimethylammonium bromide (CTAB, 99.0%), salicylic acid (technical grade, 90%), hydrogen tetrachloroaurate trihydrate (HAuCl₄·3H₂O, 99.9%), sodium borohydride (NaBH₄, 99%), trisodium citrate (98%), Na₂SO₄ (99%), NaOH (99%), carbon black (99%), sodium hypochlorite (NaClO 10% available chlorine), sodium nitroferricyanide (C₅FeN₆Na₂O, 99%), 1,3,6,8-tetra[(trimethylsilyl)ethynyl]phrene (TEP-TMS, 99%), copper(II) acetate (99%), and tetrabutylammonium

fluoride [TBAF, 1 mol·L⁻¹ in tetrahydrofuran (THF), 1 mL] were obtained from commercial sources. All chemicals were used as received. All solvents were purified according to standard procedures. Milli-Q water (18.2 $M\Omega$ ·cm resistivity at 25 °C) was used in all the experiments. All glassware was washed with aqua regia for 10 min, rinsed with water, sonicated three times for 3 min with Milli-Q water, and dried before use.

1.2 Synthesis

Preparation of Cu/Pyr-GDY: TEP-TMS (100 mg) dissolved in 20 mL THF was desilicated by TBAF (1 mol·L⁻¹ in THF, 1 mL) under N₂ atmosphere for 15 min to obtain 1,3,6,8-tetraethynylpyrene (TEP) monomer. It was washed three times with a saturated sodium chloride solution (20 mL) and was extracted with ethyl acetate (10 mL× 3). The organic phase was dried with anhydrous Na₂SO₄, after filting, and the solvent was removed under reduced pressure. The obtained TEP monomer was dissolved with 25 mL pyridine. Copper(II) acetate (30 mg) was dissolved in pyridine (5-10 mL) in a three-necked flask. The TEP solution was added dropwise into the flask at 110 °C, and the mixture was kept at the same temperature for 3 d. Pyridine was removed under reduced pressure. The obtained Cu/Pyr-GDY powder was washed with N,N-dimethylformamide (DMF), and acetone to remove unreacted TEP monomers and oligomers, and the dark brown powder was dried at 50 °C under vacuum overnight.

Preparation of Pyr-GDY: Cu/Pyr-GDY powder (50 mg), FeCl₃ solution (1 mol·L⁻¹, 100 mL), and HCl solution (1 mmol·L⁻¹, 300 mL) were mixed in a centrifuge tube, and the mixture was stirred at room temperature for 12 h. The powder was separated via centrifugation, washed three times alternately with HCl (1 mol·L⁻¹, 100 mL) and acetone (100 mL), and then Pyr-GDY was dried at 50 °C under vacuum overnight.

Preparation of Au/Pyr-GDY: according to the literature method^[57], trisodium citrate (0.375 g) and HAuCl₄·3H₂O (0.188 g) were dissolved in 15 mL ultrapure water under vigorous stirring (>1 400 r·min⁻¹). Subsequently, freshly prepared NaBH₄ (0.225 g) was added. The color of the solution changed from transparent to wine - red. After 2 min the solution was kept

under mild stirring (400 r·min⁻¹) for 6 h at room temperature. Then, 10 mg of Pyr-GDY was added, and the mixture was stirred for 6 h. It was freeze-dried, placed in a tube furnace, and heated at 200 °C for 2 h to obtain Au/Pyr-GDY.

无

机

1.3 Instrumentation

The scanning electron microscopy (SEM) images were measured using an ultrahigh-resolution scanning electron microscope with FEG (FEI, Verios 460L). The transmission electron microscopy (TEM) images were obtained using a transmission electron microscope equipped with a LaB6 Gun (Tecnai G2 Spirit TWIN, FEI, USA) at an acceleration voltage of 120 kV. The high-resolution transmission electron microscopy (HRTEM) images and the corresponding energydispersive X - ray spectroscopy (EDS) elemental mapping results were obtained using a high - resolution transmission electron microscope (Talos F200X, FEI, USA). Raman spectra were recorded using a highresolution laser confocal fiber Raman spectrometer (HORIBA EVOLVTION, HORIBA JobinYvon, France). Powder X-ray diffraction (XRD) was conducted using a Smart X-ray diffractometer (Smart Lab 9 kW, Rigaku, Japan) with Cu $K\alpha$ radiation ($\lambda = 0.154$ 178 nm). XRD's working voltage and current were 40 kV and 150 mA respectively. The diffraction data were recorded in the 2θ range of $20^{\circ}-80^{\circ}$ with a scan rate of 10 (°) · min⁻¹. X - ray photoelectron spectroscopy (XPS) was obtained using a photoelectron spectrometer (ESCALAB250Xi, THERMO SCIENTIFIC, United Kingdom), and the XPS spectra were calibrated versus C1s (284.8 eV) binding energy. The amounts of Au, Fe, and Cu on the catalysts were determined via inductively coupled plasma-atomic emission spectroscopy (ICP-MS, SPECTRO-BLUE). The BET (Brunauer-Emmett-Teller) surface area and pore size were measured using a multistation ratio surface microhole and vapor adsorption analyzer (Japan, Microtrac BEL, BELSORP-Max). FTIR spectra were recorded on a PerkinElmer Frontier Mid-IR FTIR spectrometer. The absorbance data from the spectrophotometer were measured on the Beijing General TU-1900 ultraviolet-visible (UV-Vis) spectrophotometer. The ¹H NMR spectrum was recorded with a Bruker 400 MHz spectrometer in CDCl₃. The chemical shifts (δ) of ¹H NMR were measured in ppm, referenced to the residual ¹H signal of non-deuterated DMSO (δ =2.5) as internal standards. The electrochemical experiments for NRR (N₂ reduction reaction) were conducted using a CHI660E electrochemical station. Electrolysis utilized an H-type electrolysis cell. The Ag/AgCl electrode (saturated KCl solution) and Pt foil purchased from Gaoss Union (Tianjin) Photoelectric Technology Co., Ltd., were used as the reference electrode and counter electrode, respectively.

1.4 Electrochemical NRR measurements

The electrochemical experiments were carried out on an electrochemical workstation using a three-electrode configuration with Au/Pyr-GDY as a working electrode, a Pt foil counter electrode, and an Ag/AgCl reference electrode, respectively. The reference electrodes were calibrated on a reversible hydrogen electrode (RHE).

2 Results and discussion

2.1 Structural characterizations

The results of SEM, TEM, Raman spectra, XPS, and N₂ adsorption isotherms of Cu/Pyr-GDY, Pyr-GDY, and Au/Pyr-GDY are given in Fig. S1-S6 (Supporting information), respectively. Compared with the morphology of Pyr-GDY shown in Fig. S1 and S6, the SEM image (Fig. 1a) shows a slight change in the morphology of Au/Pyr-GDY due to its annealing at 200 °C. The TEM image reveals that Au NPs were uniformly distributed on the surface of Au/Pyr-GDY, with the average size of the Au NPs being about 3.69 nm (Fig. 1b). The characteristic diffraction pattern of the HRTEM image of Au/Pyr-GDY is shown in Fig. 1c. A clear lattice fringe of 0.236 nm corresponds to the (111) crystalline plane of Au NPs was observed in Au/Pyr-GDY (Fig. 1c). The elemental mapping images (Fig. S8) of Au/ Pyr-GDY reveal that C and Au were evenly distributed throughout the sample.

There are three peaks in the Raman spectrum of Au/Pyr-GDY (Fig.1d), in which the peaks at 1 354 and 1 612 cm⁻¹ correspond to the C—H in-plane bending vibration, and the C—C stretching vibration of the

pyrene ring, respectively. The characteristic peak at 2 182 cm⁻¹, is attributed to the conjugated diacetylene links in Au/Pyr-GDY, which shifts to a lower wavenumber by 6 cm⁻¹ compared to that of Pyr-GDY (2 188 cm⁻¹, Fig. S2b). This shift may be attributed to the strong interactions between Au NPs and Pyr-GDY. The XRD pattern of Au/Pyr-GDY showed four peaks belonging to Au NPs, in which an intense diffraction peak at 38.10° corresponds to the (111) reflection of Au crystal surface, and three smaller peaks at 44.31°, 64.59°, and 77.56° correspond to the (200), (220), and (311) reflections of Au crystal surfaces, respectively (Fig. 1e). The content (mass fraction) of Au NPs in Au/Pyr-GDY was 1.72% as determined by ICP-MS analysis.

The C1s XPS (X-ray photoelectron spectroscopy) spectrum of Cu/Pyr-GDY shows a peak that can be deconvoluted into four sub-peaks at 284.6, 285.0, 286.6, and 288.5 eV, respectively (Fig. S3a), corresponding to the binding energies of C=C (sp^2), C=C (sp), C—O, and C=O bonds, respectively. The area of the sp^2 -hybridized carbon was almost twice as large as

that of the *sp*-hybridized carbon, which aligns with the ideal structure of Au/Pyr-GDY. The C1s XPS spectrum of Au/Pyr-GDY was similar to those of Cu/Pyr-GDY and Pyr-GDY, indicating the anchoring of Au NPs on Pyr-GDY did not alter its electronic state. The Au4f XPS of Au/Pyr-GDY showed two peaks at 84.4 and 87.9 eV, which corresponds to Au4f_{7/2} and Au4f_{5/2}, respectively (Fig. 1f). Compared with those of Au NPs (84.0 and 87.7 eV), the higher shifts in Au/Pyr-GDY can be attributed to the strong interactions between Au NPs and Pyr-GDY. Electron-deficient Au NPs more readily catalyze eNRR, as they can form stronger bonds with the intermediates in eNRR^[48].

The N₂ adsorption experiment was carried out at 77 K. The BET surface area and pore size of Au/Pyr-GDY were determined to be 454 m²·g⁻¹ and 3.1 nm, respectively (Fig.S5e and S5f), indicating a large surface area in the 3D sponge-like porous Pyr-GDY. In addition, the BET surface area and pore size were determined to be 465 m²·g⁻¹ and 3.8 nm for Pyr-GDY (Fig. S5c and S5d). Compared to those of Pyr-GDY, the slight decrease in BET surface area and pore size is

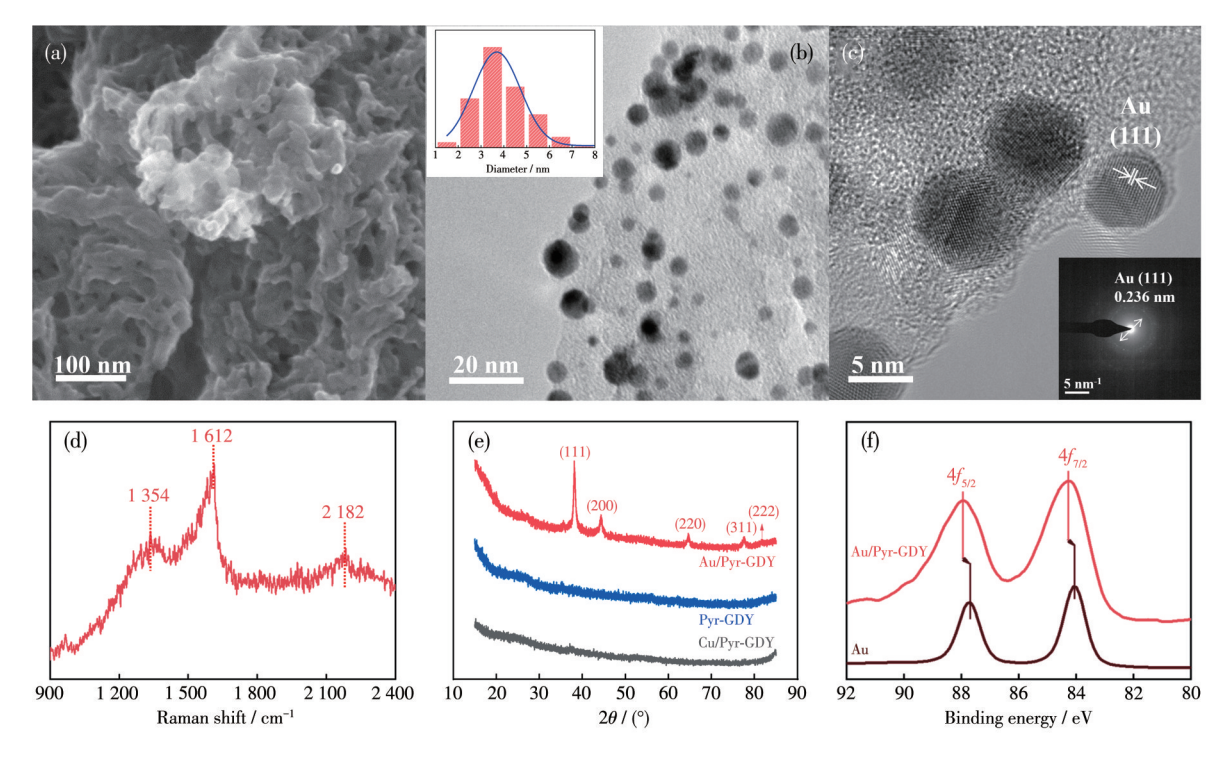


Fig.1 (a) SEM image, (b) TEM image and the histogram for the size distribution of Au NPs (Inset), (c) HRTEM image and the diffraction pattern, (d) Raman spectrum of Au/Pyr-GDY; (e) XRD patterns of Cu/Pyr-GDY, Pyr-GDY, and Au/Pyr-GDY; (f) XPS spectra for Au4f in Au/Pyr-GDY and Au

likely due to some pores being blocked by the Au NPs. Moreover, the result of infrared spectroscopy analysis (Fig. S9) shows that the surface capping agent on Au NPs was removed in Au/Pyr-GDY.

无

2.2 N₂ electroreduction

After successfully synthesizing Au/Pyr-GDY, we conducted nitrogen reduction tests by purging with argon and then nitrogen for 30 min. During the electrolysis, the H-type electrolysis cell was purged with nitrogen to ensure that the nitrogen bubbles accurately reached the working electrode. A mixture of Au/Pyr-GDY (0.8 mg·cm⁻²) and carbon black (0.8 mg·cm⁻²) was loaded onto a pre-treated carbon cloth. The experiment utilized a three-electrode configuration consisting of an Au/Pyr-GDY working electrode, a Pt foil counter electrode, and an Ag/AgCl reference electrode. All potentials in the test were converted to potentials versus RHE. The corresponding calibration curves for colorimetric ammonia and hydrazine hydrate are shown in Fig.S10 and S11.

As shown in Fig.2a, the current intensity of the N_2 -saturated electrolyte was larger than that of the Ar-saturated electrolyte, indicating that Au/Pyr-GDY exhibited eNRR activity. At -0.3 V (vs RHE), the highest NH₃ yield ($Y_{\rm NH_3}$) reached 32.1 μ g·h⁻¹·mg_{cal}⁻¹ (Fig.S12a) with a FE of 26.9% (Fig.2b), and the current intensity of -0.47 mA·cm⁻² (Fig. 2c). To confirm the origin of NH₃, three controlled experiments were conducted: (i) the working electrode in an Ar-saturated electrolyte solution at -0.3 V (vs RHE) for 2 h; (ii) The working electrode in an electrolyte with continuous N_2 flow at open circuit potential for 2 h; (iii) Bare carbon cloth in an

electrolyte with continuous N_2 flow at -0.3~V (vs RHE) for 2 h. The corresponding UV-Vis absorption spectra (Fig. S12b) indicated that a negligible amount of NH₃ product was generated under the three conditions. No hydrazine had been detected, indicating the good selectivity of the catalyst (Fig. S12c). The ^{15}N isotopic labeling experiment was further conducted to verify the original N source of the NH₃. As shown in Fig. S13, the spectra indicated a triplet coupling for $^{14}NH_4^+$ and a doublet coupling for $^{15}NH_4^+$ using $^{14}N_2$ and $^{15}N_2$ as feedstock, respectively, which was consistent with those of $^{(14}NH_4)_2SO_4$ and $^{(15}NH_4)_2SO_4$, demonstrating the production of NH₃ resulting from the electrocatalytic eNRR on Au/Pyr-GDY.

The catalysts of Au NPs anchored on the carbon black (Au/C) were also prepared for comparison. As shown in Fig.S14, though the SEM and TEM images of Au/C confirmed the presence of Au NPs on the carbon black support, the XPS spectrum of Au4f in Au/C showed that Au NPs had no interaction with the carbon black support (Fig. 3a). The XRD pattern of Au/C showed that the Au NPs on Au/C were not well crystallized (Fig. S15), with the peaks at 38.16° and 43.75° corresponding to the (111) and (200) reflections of the Au crystal surface, and an obvious peak around 24.52° corresponding to the (002) plane of graphite. In addition, the BET surface area of Au/C (87 m²·g⁻¹) was much smaller than that of Au/Pyr-GDY (Fig. S16). As expected, the N₂ electroreduction performance of Au/C was much inferior to that of Au/Pyr-GDY, with an NH3 yield of only 9.30 μg·h⁻¹·mg_{cat}⁻¹ and a FE of 11.47% at -0.2 V (vs RHE) (Fig. 3b), and a current intensity of

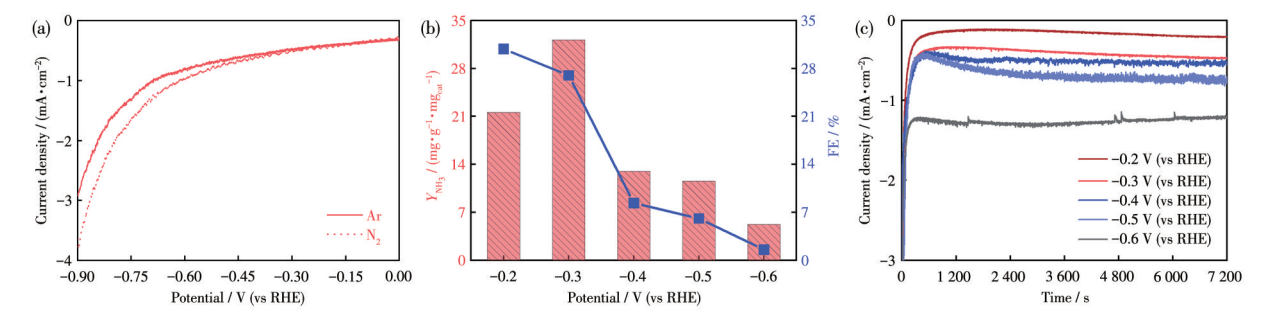


Fig.2 (a) Linear sweep voltammetry curves in Ar- and N₂-saturated 0.1 mol·L⁻¹ Na₂SO₄ solution; (b) NH₃ yield and FE at different applied potentials in 0.1 mol·L⁻¹ Na₂SO₄ solution of Au/Pyr-GDY; (c) Chronoamperometry tests with Au/Pyr-GDY electrode at various potentials from −0.2 to −0.6 V (vs RHE) in 0.1 mol·L⁻¹ Na₂SO₄ solution

only −0.34 mA·cm⁻² at −0.2 V (vs RHE) (Fig.3c). The above results indicate that Pyr-GDY is superior to carbon black as support for anchoring Au NPs and eNRR, due to the stronger Au NPs and Pyr-GDY interactions, as well as the larger BET surface area. Moreover, it was found that Au/Pyr-GDY could be stable for more than 22 h (Fig.4a) and five cycles (Fig.4b). After the cyclic test, the morphology of Au/Pyr-GDY had been main-

tained, the Au NPs in Au/Pyr-GDY had not been aggregated (Fig.S17). In addition, the characteristic peaks in Raman spectroscopy (Fig. S18a) and XRD remained unchanged (Fig.S18b). In contrast, the morphology of Au/C after eNRR indicated that the Au NPs were aggregated due to the weak Au-C interactions in Au/C (Fig.S19).

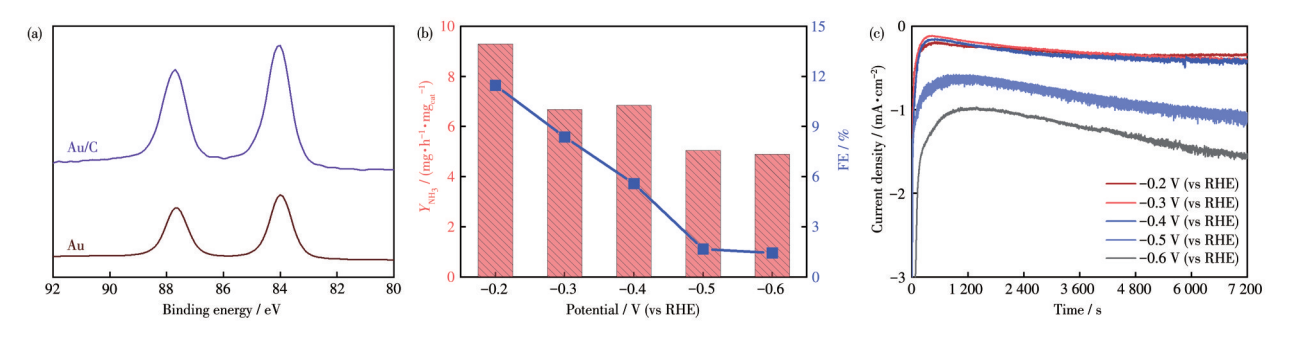


Fig.3 (a) XPS spectra of Au4f for Au/C and Au; (b) NH₃ yields and FE of Au/C at different applied potentials in 0.1 mol⋅L⁻¹ Na₂SO₄ solution; (c) Chronoamperometry tests of Au/C at various potentials from −0.2 to −0.6 V (vs RHE) in 0.1 mol⋅L⁻¹ Na₂SO₄ solution

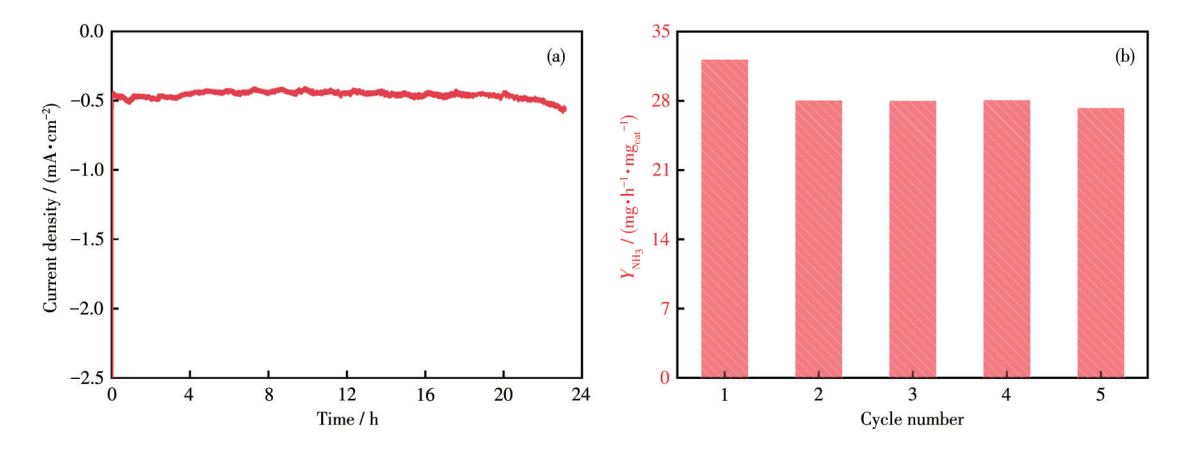


Fig.4 (a) Stability test and (b) cycling test of Au/Pyr-GDY catalyst at -0.3 V (vs RHE)

3 Conclusions

Pyr-GDY with rich alkyne groups can act as an excellent support for anchoring and stabilizing small Au NPs through strong Au/Pyr-GDY interaction, with an average size of 3.69 nm. The strong interactions between Au NPs and Pyr-GDY also lead to Au NPs' electron deficiency due to the electron-deficient nature of alkyne groups, which could form stronger bonds with the intermediates during eNRR. In addition, the spongelike porous Pyr-GDY possessed a large BET surface which is beneficial for eNRR. As a result, Au/Pyr-GDY

exhibited good electrocatalytic performance for N_2 reduction to NH_3 , with an NH_3 yield of 32.1 $\mu g \cdot h^{-1} \cdot mg_{cat}^{-1}$, and a FE of 26.9% at -0.3 V (vs RHE). Au/Pyr-GDY had good durability during long-term electrolysis. This paper demonstrates that GDY-based materials are excellent supports for anchoring and stabilizing small metal NPs for efficient catalysis of N_2 electroreduction.

Acknowledgments: This work was financially supported by the National Natural Science Foundation of China (Grants No. U21A20286, 21931007).

Supporting information is available at http://www.wjhxxb.cn

References:

- [1]BROWN K A, HARRIS D F, WILKER M B, RASMUSSEN A, KHADKA N, HAMBY H, KEABLE S, DUKOVIC G, PETERS J W, SEEFELDT L C, KING P W. Light-driven dinitrogen reduction catalyzed by a CdS: Nitrogenase MoFe protein biohybrid[J]. Science, 2016, 352(6284):448-450
- [2]CHEN J G, CROOKS R M, SEEFELDT L C, BREN K L, BULLOCK R M, DARENSBOURG M Y, HOLLAND P L, HOFFMAN B, JANIK M J, JONES A K, KANATZIDIS M G, KING P, LANCASTER K M, LYMAR S V, PFROMM P, SCHNEIDER W F, SCHROCK R R. Beyond fossil fuel-driven nitrogen transformations[J]. Science, 2018, 360(6391):eaar6611
- [3]ROSCA V, DUCA M, DE GROOT M T, KOPER M T M. Nitrogen cycle electrocatalysis[J]. Chem. Rev., 2009,109(6):2209-2244
- [4]ASHIDA Y, ARASHIBA K, NAKAJIMA K, NISHIBAYASHI Y. Molybdenum-catalysed ammonia production with samarium diiodide and alcohols or water[J]. Nature, 2019,568(7753):536-540
- [5]VAN KESSEL M A H J, SPETH D R, ALBERTSEN M, NIELSEN P H, OP DEN CAMP H J M, KARTAL B, JETTEN M S M, LUCKER S. Complete nitrification by a single microorganism[J]. Nature, 2015,528 (7583):555-559
- [6]TALUKDAR B, KUO T C, SNEED B Y, LYU L M, LIN H M, CHUANG Y C, CHENG M J, KUO C H. Enhancement of NH₃ production in electrochemical N₂ reduction by the Cu-rich inner surfaces of beveled CuAu nanoboxes[J]. ACS Appl. Mater. Interfaces, 2021, 13 (44):51839-51848
- [7]VAN DAMME M, CLARISSE L, WHITBURN A, HADJI-LAZARO J, HURTMANS D, CLERBAUX C, COHEUR P F. Industrial and agricultural ammonia point sources exposed[J]. Nature, 2018, 564(7734): 99-103
- [8]LÉGARÉ M A, BÉLANGER-CHABOT G, DEWHURST R D, WELZ E, KRUM-MENACHER I, ENGELS B, BRAUNSCHWEIG H. Nitrogen fixation and reduction at boron[J]. Science, 2018,359(6378):896-900
- [9]ZHANG H R, WANG H J, CAO X Q, CHEN M D, LIU Y L, ZHOU Y T, HUANG M, XIA L, WANG Y, LI T D, ZHENG D D, LUO Y S, SUN S J, ZHAO X, SUN X P. Unveiling cutting-edge developments in electrocatalytic nitrate-to-ammonia conversion[J]. Adv. Mater., 2024, 36(16):2312746
- [10]HUANG Z L, RAFIQ M, WOLDU A R, TONG Q X, ASTRUC D, HU L S. Recent progress in electrocatalytic nitrogen reduction to ammonia (NRR)[J]. Coord. Chem. Rev., 2023,478:214981
- [11]MICHALSKY R, AVRAM A M, PETERSON B A, PFROMM P H, PETERSON A A. Chemical looping of metal nitride catalysts: Lowpressure ammonia synthesis for energy storage[J]. Chem. Sci., 2015,6 (7):3965-3974
- [12]FOSTER S L, BAKOVIC S I P, DUDA R D, MAHESHWARI S, MILTON R D, MINTEER S D, JANIK M J, RENNER J N,

- GREENLEE L F. Catalysts for nitrogen reduction to ammonia[J]. Nat. Catal., 2018,1(7):490-500
- [13]MARTÍN A J, SHINAGAWA T, PÉREZ-RAMÍREZ J. Electrocatalytic reduction of nitrogen: From haber-bosch to ammonia artificial leaf[J]. Chem, 2019,5(2):263-283
- [14]IULIANELLI A, LIGUORI S, WILCOX J, BASILE A. Advances on methane steam reforming to produce hydrogen through membrane reactors technology: A review[J]. Catal. Rev., 2016,58(1):1-35
- [15]CHOI C, BACK S, KIM N Y, LIM J, KIM Y H, JUNG Y. Suppression of hydrogen evolution reaction in electrochemical $\rm N_2$ reduction using single atom catalysts: A computational guideline[J]. ACS Catal., 2018,8(8):7517-7525
- [16]DONG K, YAO Y C, LI H B, LI H J W, SUN S J, HE X, WANG Y, LUO Y S, ZHENG D D, LIU Q, LI Q, MA D W, SUN X P, TANG B. H₂O₂-mediated electrosynthesis of nitrate from air[J]. Nat. Synthesis, 2024,3:763-773
- [17]LI S X, LIANG J, WEI P P, LIU Q, XIE L S, LUO Y L, SUN X P. ITO@TiO₂ nanoarray: An efficient and robust nitrite reduction reaction electrocatalyst toward NH₃ production under ambient conditions [J]. eScience, 2022,2(4):382-388
- [18]HAN J R, LIU Z C, MA Y J, CUI G W, XIE F Y, WANG F X, WU Y P, GAO S Y, XU Y H, SUN X P. Ambient N₂ fixation to NH₃ at ambient conditions: Using Nb₂O₅ nanofiber as a high-performance electrocatalyst[J]. Nano Energy, 2018,52:264-270
- [19]LU Y H, YANG Y, ZHANG T F, GE Z, CHANG H C, XIAO P S, XIE Y Y, HUA L, LI Q Y, LI H Y, MA B, GUAN N J, MA Y F, CHEN Y S. Photoprompted hot electrons from bulk cross-linked graphene materials and their efficient catalysis for atmospheric ammonia synthesis[J]. ACS Nano, 2016,10(11):10507-10515
- [20]SHIPMAN M A, SYMES M D. Recent progress towards the electrosynthesis of ammonia from sustainable resources[J]. Catal. Today, 2017,268:57-68
- [21]SHE Z W, KIBSGAARD J, DICKENS C F, CHORKENDORFF I, NORSKOV J K, JARAMILLO T F. Combining theory and experiment in electrocatalysis: Insights into materials design[J]. Science, 2017,355(6321):eaad4998
- [22]PANG Y P, SU C, JIA G H, XU L Q, SHAO Z P. Emerging two-dimensional nanomaterials for electrochemical nitrogen reduction[J]. Chem. Soc. Rev., 2021,50(22):12744-12787
- [23]ZHONG Y, XIONG H L, LOW J X, LONG R, XIONG Y J. Recent progress in electrochemical C—N coupling reactions[J]. eScience, 2023,3(1):100086
- [24]LI Z, ATTANAYAKE N H, BLACKBURN J L, MILLER E M. Carbon dioxide and nitrogen reduction reactions using 2D transition metal dichalcogenide (TMDC) and carbide/nitride (MXene) catalysts [J]. Energy Environ. Sci., 2021,14(12):6242-6286
- [25]JIANG Y, FU H, LIANG Z, ZHANG Q, DU Y P. Rare earth oxide based electrocatalysts: Synthesis, properties and applications[J]. Chem. Soc. Rev., 2024,53(2):714-763
- [26]TIAN D, DENNY S R, LI K, WANG H, KATTEL S, CHEN J G. Density functional theory studies of transition metal carbides and

- nitrides as electrocatalysts[J]. Chem. Soc. Rev., 2021,50(22):12338-12376
- [27]OUYANG L, LIANG J, LUO Y S, ZHENG D D, SUN S J, LIU Q, HAMDY M S, SUN X P, YING B W. Recent advances in electrocatalytic ammonia synthesis[J]. Chin. J. Catal., 2023,50:6-44
- [28]MUSHTAQ M A, KUMAR A, LIU W, JI Q Q, DENG Y G, YASIN G, SAAD A, RAZA W, ZHAO J, AJMAL S, WU Y Y, AHMAD M, LASHARI N U R, WANG Y, LI T S, SUN S J, ZHENG D D, LUO Y S, CAI X K, SUN X P. A metal coordination number determined catalytic performance in manganese borides for ambient electrolysis of nitrogen to ammonia[J]. Adv. Mater., 2024,36(21):2313086
- [29]TAO H C, CHOI C, DING L X, JIANG Z, HAN Z, JIA M W, FAN Q, GAO Y N, WANG H H, ROBERTSON A W, HONG S, JUNG Y S, LIU S Z, SUN Z Y. Nitrogen fixation by Ru single-atom electrocatalytic reduction[J]. Chem, 2019,5(1):204-214
- [30]WANG H J, LI Y H, LI C J, DENG K, WANG Z Q, XU Y, LI X N, XUE H R, WANG L. One-pot synthesis of bi-metallic PdRu tripods as an efficient catalyst for electrocatalytic nitrogen reduction to ammonia[J]. J. Mater. Chem. A, 2019,7(2):801-805
- [31]WANG X J, LUO M, LAN J, PENG M, TAN Y W. Nanoporous intermetallic Pd₃Bi for efficient electrochemical nitrogen reduction[J]. Adv. Mater., 2021,33(18):2007733
- [32]LIU H M, HAN S H, ZHAO Y, ZHU Y Y, TIAN X L, ZENG J H, JIANG J X, XIA B Y, CHEN Y. Surfactant-free atomically ultrathin rhodium nanosheet nanoassemblies for efficient nitrogen electroreduction[J]. J. Mater. Chem. A, 2018,6(7):3211-3217
- [33]LI S J, BAO D, SHI M M, WULAN B R, YAN J M, JIANG Q. Amorphizing of Au nanoparticles by ${\rm CeO_x}$ -RGO hybrid support towards highly efficient electrocatalyst for N₂ reduction under ambient conditions[J]. Adv. Mater., 2017,29(33):1700001
- [34]BAO D, ZHANG Q, MENG F L, ZHONG H X, SHI M M, ZHANG Y, YAN J M, JIANG Q, ZHANG X B. Electrochemical reduction of N₂ under ambient conditions for artificial N₂ fixation and renewable energy storage using N₂/NH₃ cycle[J]. Adv. Mater., 2017, 29(3): 1604799
- [35]NAZEMI M, PANIKKANVALAPPIL S R, EL-SAYED M A. Enhancing the rate of electrochemical nitrogen reduction reaction for ammonia synthesis under ambient conditions using hollow gold nanocages [J]. Nano Energy, 2018,49:316-323
- [36]ZHENG J Y, LYU Y H, QIAO M, WANG R L, ZHOU Y Y, LI H, CHEN C, LI Y F, ZHOU H J, JIANG S P, WANG S Y. Photoelectrochemical synthesis of ammonia on the aerophilic-hydrophilic heterostructure with 37.8% efficiency[J]. Chem., 2019,5(3):617-633
- [37]WANG H J, YU H J, WANG Z Q, LI Y H, XU Y, LI X, XUE H R, WANG L. Electrochemical fabrication of porous Au film on Ni foam for nitrogen reduction to ammonia[J]. Small, 2019,15(6):1804769
- [38]ZHANG J C, ZHAO B, LIANG W K, ZHOU G S, LIANG Z Q, WANG Y W, QU J Y, SUN Y H, JIANG L. Three-phase electrolysis by gold nanoparticle on hydrophobic interface for enhanced electrochemical nitrogen reduction reaction[J]. Adv. Sci., 2020, 7(22): 2002630

- [39]HE H M, ZHU Q Q, YAN Y, ZHANG H W, HAN Z Y, SUN H M, CHEN J, LI C P, ZHANG Z H, DU M. Metal-organic framework supported Au nanoparticles with organosilicone coating for high-efficiency electrocatalytic N₂ reduction to NH₃[J]. Appl. Catal. B-Environ., 2022,302:120840
- [40]ZHAO L, ZHOU J Z, ZHANG L W, SUN X, SUN X J, YAN T, REN X, WEI Q. Anchoring Au(111) on a bismuth sulfide nanorod: Boosting the artificial electrocatalytic nitrogen reduction reaction under ambient conditions[J]. ACS Appl. Mater. Interfaces, 2020, 12(50): 55838-55843
- [41]LIU D, ZHANG G, JI Q H, ZHANG Y Y, LI J H. Synergistic electrocatalytic nitrogen reduction enabled by confinement of nanosized Au particles onto a two-dimensional Ti₃C₂ substrate[J]. ACS Appl. Mater. Interfaces, 2019,11(29):25758-25765
- [42]YAO J X, ZHOU Y T, YAN J M, JIANG Q. Regulating Fe₂(MoO₄)₃ by Au nanoparticles for efficient N₂ electroreduction under ambient conditions[J]. Adv. Energy Mater., 2021,11(14):2003701
- [43]HUI L, XUE Y R, YU H D, LIU Y X, FANG Y, XING C Y, HUANG B L, LI Y L. Highly efficient and selective generation of ammonia and hydrogen on a graphdiyne-based catalyst[J]. J. Am. Chem. Soc., 2019,141(27):10677-10683
- [44]GARRIDO-BARROS P, DEROSA J, CHALKLEY M J, PETERS J C. Tandem electrocatalytic $\rm N_2$ fixation via proton-coupled electron transfer[J]. Nature, 2022,609(7925):71-76
- [45]WANG H L, YANG D D, LIU S L, YIN S L, YU H J, XU Y, LI X N, WANG Z Q, WANG L. Amorphous sulfur decorated gold nanowires as efficient electrocatalysts toward ambient ammonia synthesis[J]. ACS. Sustain. Chem. Eng., 2019,7(24):19969-19974
- [46]WANG Z Q, LI Y H, YU H J, XU Y, XUE H R, LI X N, WANG H J, WANG L. Ambient electrochemical synthesis of ammonia from nitrogen and water catalyzed by flower - like gold microstructures[J]. ChemSusChem. 2018,11(19):3480-3485
- [47]WANG H, WANG L, WANG Q, YE S Y, SUN W, SHAO Y, JIANG Z P, QIAO Q, ZHU Y M, SONG P F, LI D B, HE L, ZHANG X H, YUAN J Y, WU T, OZIN G A. Ambient electrosynthesis of ammonia: Electrode porosity and composition engineering[J]. Angew. Chem.—Int. Edit., 2018,57(38):12360-12364
- [48]ZHENG J Y, LYU Y H, QIAO M, VEDER J P, MARCO R D, BRAD-LEY J, WANG R L, LI Y F, HUANG A B, JIANG S P, WANG S Y. Tuning the electron localization of gold enables the control of nitrogen-to-ammonia fixation[J]. Angew. Chem.—Int. Edit., 2019,58 (51):18604-18609
- [49]LI G, LI Y, LIU H, GUO Y, LI Y, ZHU D. Architecture of graphdiyne nanoscale films[J]. Chem. Commun., 2010,46(19):3256-3258
- [50]LU T T, WANG H. Graphdiyne supported metal electrocatalysts: From nanoparticles and cluster to single atoms[J]. Nano Res., 2022, 15(11):9764-9778
- [51]YU H D, XUE Y R, HUI L, ZHANG C, FANG Y, LIU Y X, CHEN X, ZHANG D Y, HUANG B L, LI Y. Graphdiyne-based metal atomic catalysts for synthesizing ammonia[J]. Natl. Sci. Rev., 2021, 8(8): nwaa213

- [52]FANG Y, XUE Y R, HUI L, YU H D, LI Y L. Graphdiyne@janus magnetite for photocatalytic nitrogen fixation[J]. Angew. Chem.-Int. Edit., 2021,60(6):3170-3174
- [53]QI L, GAO Y Q, GAO Y, ZHENG Z Q, LUAN X Y, ZHAO S Y, CHEN Z Y, LIU H M, XUE Y R, LI Y L. Controlled growth of metal atom arrays on graphdiyne for seawater oxidation[J]. J. Am. Chem. Soc., 2024,146(8):5669-5677
- [54]YANG L L, WANG H J, WANG J, LI Y, ZHANG W, LU T B. A graphdiyne - based carbon material for electroless deposition and stabilization of sub-nanometric Pd catalysts with extremely high catalytic activity[J]. J. Mater. Chem. A, 2019,7(21):13142-13148
- [55]LI M, WANG H J, ZHANG C, CHANG Y B, LI S J, ZHANG W, LU T B. Enhancing the photoelectrocatalytic performance of metal-free graphdiyne-based catalyst[J]. Sci. China-Chem., 2020,63(8):1040-1045
- [56] LIU C, ZHANG C, LU T B. Graph diyne anchored ultrafine Ag nanoparticles for highly efficient and solvent-free catalysis of $\rm CO_2$ cycloaddition [J]. Mater. Chem. Front., 2021,5(16):6052-6060
- [57]SCARABELLI L, SÁNCHEZ IGLESIAS A, PÉREZ JUSTE J, LIZ-MARZÁN L M. A "tips and tricks" practical guide to the synthesis of gold nanorods[J]. J. Phys. Chem. Lett., 2015, 6(21): 4270-4279